Rare Metal Materials and Engineering
Volume 52, Issue 12, December 2023
Available online at www.rmme.ac.cn

Science Press

Cite this article as: Gao Li, Xin Xiangyang, Liu Zili, et al. Martensitic Transformation, Mechanical Properties and Corrosion Resistance of $Ni_{48}Co_1Mn_{37}In_{14-x}Al_x$ Magnetic Shape Memory Alloys[J]. Rare Metal Materials and Engineering, 2023, 52(12): 4021-4028. DOI: 10.12442/j.issn.1002-185X.E20230016.

ARTICLE

Martensitic Transformation, Mechanical Properties and Corrosion Resistance of $Ni_{48}Co_1Mn_{37}In_{14-x}Al_x$ Magnetic Shape Memory Alloys

Gao Li, Xin Xiangyang, Liu Zili, Hu Shaohui, Liao Huayu, Xu Yangrui

College of Engineering Science and Technology, Shanghai Ocean University, Shanghai 201306, China

Abstract: The effect of Al doping on microstructure, crystal structure, martensitic transformation, mechanical properties and corrosion resistance of $Ni_{48}Co_1Mn_{37}In_{14-x}Al_x$ ($0 \leqslant x \leqslant 2$) magnetic shape memory alloys was studied by the material preparation method of arc melting. The results show that the grain size of the alloy is reduced by replacing part of In with Al, and the average grain size is reduced to about 10 μm when 2at% Al element is doped, which is about 1/35 of that of the undoped sample. When the doping amount of Al is 0.25at%–2at%, the metal Al is completely dissolved into the matrix, and the solid solubility of Al in the alloy increases with the increase in the doping amount; when the doping amount is 2at%, the solid solubility of Al in the matrix is close to 2at%. With the substitution of Al for In, the alloy changes from the two-phase structure of $L2_1$ cubic austenite and monoclinic 6M martensite to a single 6M at room temperature, the unit cell volume gradually decreases, and the martensitic transformation temperature shows an upward trend. The compressive strength of the alloy continues to increase, and compared with that of $Ni_{48}Co_1Mn_{37}In_{14}$, the compressive fracture strength of $Ni_{48}Co_1Mn_{37}In_{12}Al_2$ is increased by 160%, and the compressive strain also increases from 5.46% to 6.36%. After an appropriate amount of Al replacing In, the corrosion resistance of the alloy in artificial seawater generally shows an increasing trend. The corrosion resistance of $Ni_{48}Co_1Mn_{37}In_{12}Al_2$ alloy is significantly higher than that of $Ni_{48}Co_1Mn_{37}In_{14}$ alloy, and its corrosion resistance is close to that of 304 stainless steel.

Key words: magnetic shape memory alloy; metal Al doping; martensitic transformation; mechanical properties; corrosion resistance

Martensitic transformation, as the physical basis of shape memory alloys, has been applied in human life. Shape memory alloys have developed into intelligent materials, and shows broad application prospects in the field of intelligent technology in the future thanks to the research on the martensitic transformation[1]. Since Kainuma et al[2] reported the usage of magnetic field to drive the martensitic transformation of single crystal $Ni_{45}Co_5Mn_{36.7}In_{13.3}$ alloy in 2006, magnetic field has become a new variable for regulating shape memory alloys. Based on the phase transformation behavior, magnetic shape memory alloys exhibit different physical effects such as magnetic driving strain[3–5], magnetic resistance[6–7] and magnetocaloric effect[8–10], which are expected to be applied to magnetic actuators, magnetic sensors and magnetic refrigeration. For half a century, Heusler alloy as the mainstream system of magnetic phase change materials has been continuously studied, and Ni-Mn-In alloy has become a research hotspot due to its excellent magnetic control performance. The "ferromagnetic activation effect" of Co element greatly increases the saturation magnetization difference between austenite and martensite and promotes the development of Ni-Mn-In based magnetic memory alloy[11–12]. Nowadays, shape memory alloy materials have been widely used in ocean, aviation and aerospace, biomedical and other fields. Accordingly, magnetic memory alloys also play an important role in ships, micro-aircrafts and aerospace scenes. Traditional memory alloy materials have low electrochemical stability and poor corrosion resistance[13]. In order to better resist the electrochemical corrosion damage caused by sea salt fog and air acidic pollutants[14] and to reduce the economic losses caused by corrosion failure, it is urgent to develop new memory alloy materials with excellent corrosion resistance[15].

Received date: June 09, 2023
Foundation item: National Natural Science Foundation of China (51401122, 51671126)
Corresponding author: Gao Li, Ph. D., Professor, College of Engineering Science and Technology, Shanghai Ocean University, Shanghai 201306, P. R. China, E-mail: lgao@shou.edu.cn

At the same time, good mechanical stability and machinability are the prerequisites for the application of magnetic memory alloys. Magnetic memory alloys have intrinsic brittleness of intermetallic compounds[16], so researchers try to break through this bottleneck using various methods. Recently, Matyja et al[17] increased the compressive strength of $Ni_{45.5}Co_{4.5}Mn_{36.6}In_{13.4}$ polycrystalline alloy from 260 MPa to 1250 MPa by combining mechanical alloying with the vacuum arc melting method. In addition, Bai et al[18] studied $Ni_{43.75}Mn_{37.5}In_{12.5}Co_{6.25}$ alloy with compressive strength up to 1440 MPa by spark plasma sintering. However, compared with expensive high-tech, low-cost element doping is the key to the industrial application of alloys. Previous studies have shown that when Sn is replaced by 1at% Al in $Ni_{40}Co_{10}Mn_{40}Sn_{10}$ alloy, the thermal hysteresis of the alloy decreases from 33 K to 13 K, the difference in magnetization between high-temperature and low-temperature phases remains at 100 $A\cdot m^2/kg$, and the conservative magnetic entropy changes to 30.5 $J\cdot kg^{-1}\cdot K^{-1}$ under 5 T magnetic field. Cong et al[19] investigated the mechanical properties of $Ni_{40}Co_{10}Mn_{40}Sn_9Al_1$ alloy. The compressive fracture strain reaches 8.7% and the compressive strength is as high as 1050 MPa at room temperature. The excellent mechanical properties are extremely beneficial to the potential magnetocaloric applications. Moreover, Al is a metal with good corrosion resistance, and it reacts with oxygen in the air to form a dense alumina film, which plays a protective role in the matrix alloy. In this study, the microstructure, martensitic transformation, mechanical properties and corrosion resistance of $Ni_{48}Co_1Mn_{37}In_{14}$ alloy with partial In substituted by Al were investigated by element doping, which provides an experimental basis for the design of new high-performance Ni-Mn-In magnetic memory alloys.

1 Experiment

Ni, Co, Mn, In and Al elements with purity above 99.99% were used as the ingredients according to the nominal composition of $Ni_{48}Co_1Mn_{37}In_{14-x}Al_x$ (x=0, 0.25, 0.5, 0.75, 1, 2, at%) alloy. The samples were prepared in a WK-II type non-consumable vacuum arc furnace filled with high-purity argon and repeatedly melted four times to obtain round ingots with uniform composition. After cooling, the alloy block was sealed in a vacuum quartz tube filled with argon for annealing treatment. The alloy block was held at 1173 K for 24 h and then quenched with water to obtain higher order.

The HA400 WEDM machine was used to obtain samples that meet the test requirements. The microstructure of the alloy was observed by Olympus metallographic microscope and Hitachi S-4800 scanning electron microscope (SEM) equipped with energy dispersive spectroscopy (EDS). Five points were selected for testing on each sample, and the average value was taken as the result of the final composition ratio. The phase composition and crystal structure were analyzed by LabX XRD-6100 X-ray diffractometer (XRD). The test angle was 20° – 100°, and the scanning rate was 2°/min. The martensitic transformation temperature was measured by Perkin-Emer diamond differential scanning calorimetry (DSC). The test temperature was 200–500 K, and the heating and cooling rates were 10 K/min. The room temperature compression test was carried out on the CSS-43300 electronic universal mechanical testing machine. The sample size was Φ3 mm×5 mm cylinder, and the compression rate was 0.1 mm/min. The fracture morphology was observed by SEM. The working face of 1 cm^2 was left after the alloy sample was encapsulated with epoxy resin. The corrosion resistance of the alloy in artificial seawater solution was studied by Reference 600+ electrochemical workstation. Three groups of parallel samples were selected, and each sample was tested twice to reduce the experimental error.

2 Results and Discussion

2.1 Microstructure of $Ni_{48}Co_1Mn_{37}In_{14-x}Al_x$ alloys

Fig.1 is the optical micrograph of $Ni_{48}Co_1Mn_{37}In_{14-x}Al_x$ (x=0, 0.25, 0.5, 2, at%) alloys. Fig.1a is the optical microstructure of undoped Al alloy at room temperature. The austenite phase shows coarse equiaxed crystal morphology, clear grain boundary, and large grain size. After doping with 0.25at% Al, the alloy grains are regular polygons, and the average size is reduced from 350 μm to about 100 μm. The martensitic transformation occurs in the alloy at room temperature. When the Al content reaches 2at%, the average grain size of the alloy decreases to about 10 μm. As shown in Fig. 1d, the higher the Al content, the better the grain refinement effect, and the grain size tends to be consistent. The grain refinement mechanism of Al is mainly manifested in the process of the solid solution of Al with a small atomic radius to the matrix by introducing chemical pressure, resulting in a certain degree of grain boundary drag, inhibiting grain boundary movement and hindering grain growth.

Table 1 shows the results of energy spectrum analysis for $Ni_{48}Co_1Mn_{37}In_{14-x}Al_x$ (x=0, 0.25, 0.5, 0.75, 1, 2, at%) alloys. The energy spectrum data show that the solid solubility of Al in the alloy increases with the increase in Al content. When 2at% Al is used to replace In, the solid solubility of Al in the matrix is close to 2at%.

Fig.2 shows the XRD patterns of $Ni_{48}Co_1Mn_{37}In_{14-x}Al_x$ alloy at room temperature. It can be seen that the Ni-Co-Mn-In alloy in this study is a mixed structure of $L2_1$ cubic austenite and monoclinic 6M modulated martensite at room temperature. After doping of Al instead of In, the crystal structure of the alloy changes from two-phase coexistence to a single 6M martensite. As seen from the position of the diffraction peak, with the increase in Al element, the position of the diffraction peak moves to a high angle. When the Al content increases to 1at%, the main peak angle increases from 38.16° without doping to 42.8°. This shows that the substitution of Al for In makes the lattice of $Ni_{48}Co_1Mn_{37}In_{14-x}Al_x$ alloy shrink and the cell volume decreases, so that the diffraction peak moves to the right because the radius of the Al atom is smaller than that of In atom[20]. The intensity of the diffraction peak mainly depends on the grain size. The finer the grain, the thinner the peak width and the higher the peak.

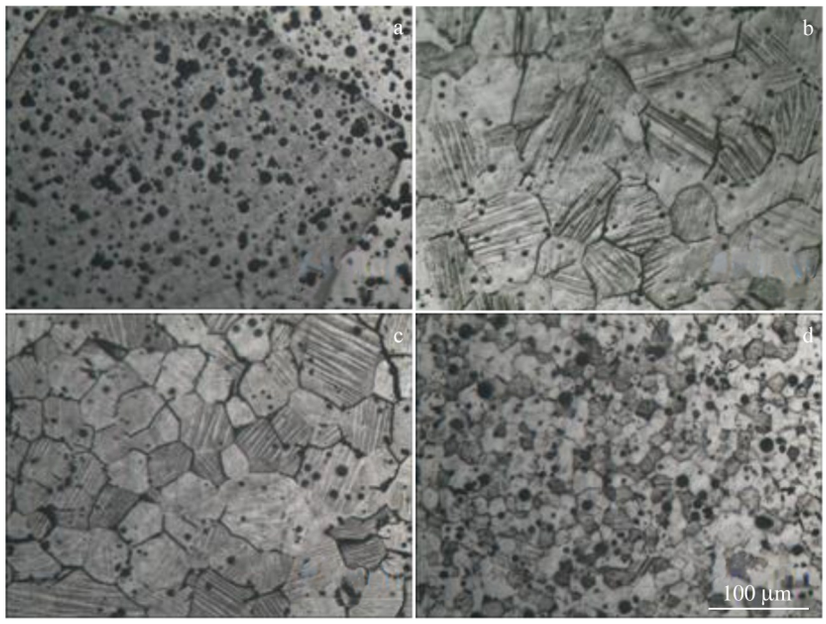

Fig.1 Optical microscope microstructures of $Ni_{48}Co_1Mn_{37}In_{14-x}Al_x$ alloys: (a) x=0, (b) x=0.25, (c) x=0.5, and (d) x=2

Table 1 EDS results of $Ni_{48}Co_1Mn_{37}In_{14-x}Al_x$ alloys (at%)

Composition	Ni	Co	Mn	In	Al
$Ni_{48}Co_1Mn_{37}In_{14}$	48.6	0.9	36.9	13.6	-
$Ni_{48}Co_1Mn_{37}In_{13.75}Al_{0.25}$	48.3	0.9	36.4	13.9	0.5
$Ni_{48}Co_1Mn_{37}In_{13.5}Al_{0.5}$	49.1	0.8	36.8	13.4	0.7
$Ni_{48}Co_1Mn_{37}In_{13.25}Al_{0.75}$	47.8	0.9	36.5	13.3	0.7
$Ni_{48}Co_1Mn_{37}In_{13}Al_1$	48.6	0.8	37.0	12.6	1.1
$Ni_{48}Co_1Mn_{37}In_{12}Al_2$	48.8	1.1	36.9	11.3	2.0

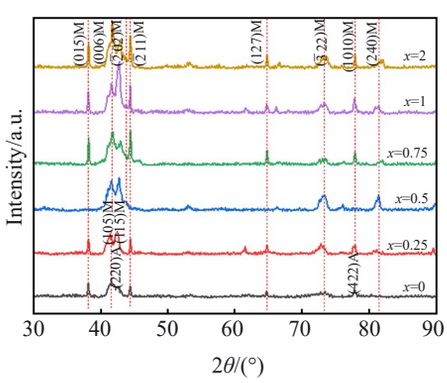

Fig.2 XRD patterns of $Ni_{48}Co_1Mn_{37}In_{14-x}Al_x$ alloys at room temperature

It can be seen that the microstructures of alloys with 1at% and 2at% Al are relatively dense.

We calculated the lattice constant and cell volume using the Bragg equation. Table 2 shows the lattice constant and cell volume of each component. It can be seen that the lattice constants of $Ni_{48}Co_1Mn_{37}In_{14}$ alloy are a=0.439 nm, b=0.570 nm, c=1.296 nm and β=93.18°. With the doping of trace Al, the austenite phase of the alloy disappears, and the monoclinic 6M modulation structure of the martensite phase remains unchanged. The lattice constants a, c and angle β remain roughly unchanged, while the value of b decreases, resulting in a decrease in cell volume. When the Al content increases to 2at%, the cell volume decreases from 323.94×10^{-3} nm^3 to 318.39×10^{-3} nm^3, about 2% smaller than that of the undoped sample. It is known that the atomic radius of Al is smaller than that of In, and the doping of Al will lead to decrease in Mn-Mn atomic spacing. Therefore, the cell volume of the alloy decreases in the process of replacing In with Al.

2.2 Martensitic transformation of $Ni_{48}Co_1Mn_{37}In_{14-x}Al_x$ alloys

Fig. 3 shows the DSC test results of $Ni_{48}Co_1Mn_{37}In_{14-x}Al_x$ alloys. As shown in Fig. 3a–3f, there is a sharp peak in the curve during the heating and cooling process, indicating that the doping of Al maintains the one-step thermoelastic martensitic transformation characteristics of the alloy. In addition, in Fig. 3a, 3e, and 3f, additional prismatic undulations can be observed, with weak peaks and small hysteresis, which is a typical second-order phase change feature, indicating that Curie transformation occurs. Different from the general non-magnetic element doping, the Curie temperature of the alloy with Al content no more than 2at% shows an upward trend. When the doping amount of Al is 2at%, the Curie temperature of the alloy reaches 376 K, which is 50 K higher than that of the undoped alloy. The specific reason for this phenomenon is under study.

The temperatures of martensite start (M_s) and end (M_f), austenite start (A_s) and end (A_f) were measured by tangent method and listed in Table 3. The thermal hysteresis ΔT_{hys} caused by structural transformation is calculated by formula $\Delta T_{hys}= [(A_f - M_s) + (A_s - M_f)]/2$. The thermal hysteresis of $Ni_{48}Co_1Mn_{37}In_{14}$ alloy is about 10 K. After doping with 0.5at% Al, the thermal hysteresis of the alloy sample is slightly

Table 2 Cell parameters of $Ni_{48}Co_1Mn_{37}In_{14-x}Al_x$ alloys

x	a/×10^{-1} nm	b/×10^{-1} nm	c/×10^{-1} nm	V_m/×10^{-3} nm^3	β/(°)	Room temperature phase
0	4.39	5.70	12.96	323.94	93.18	6M+A
0.25	4.40	5.63	12.98	320.79	93.46	6M
0.5	4.38	5.61	13.03	319.36	93.91	6M
0.75	4.40	5.63	12.97	320.55	92.73	6M
1	4.43	5.55	13.02	319.66	91.34	6M
2	4.39	5.59	13.01	318.39	94.11	6M

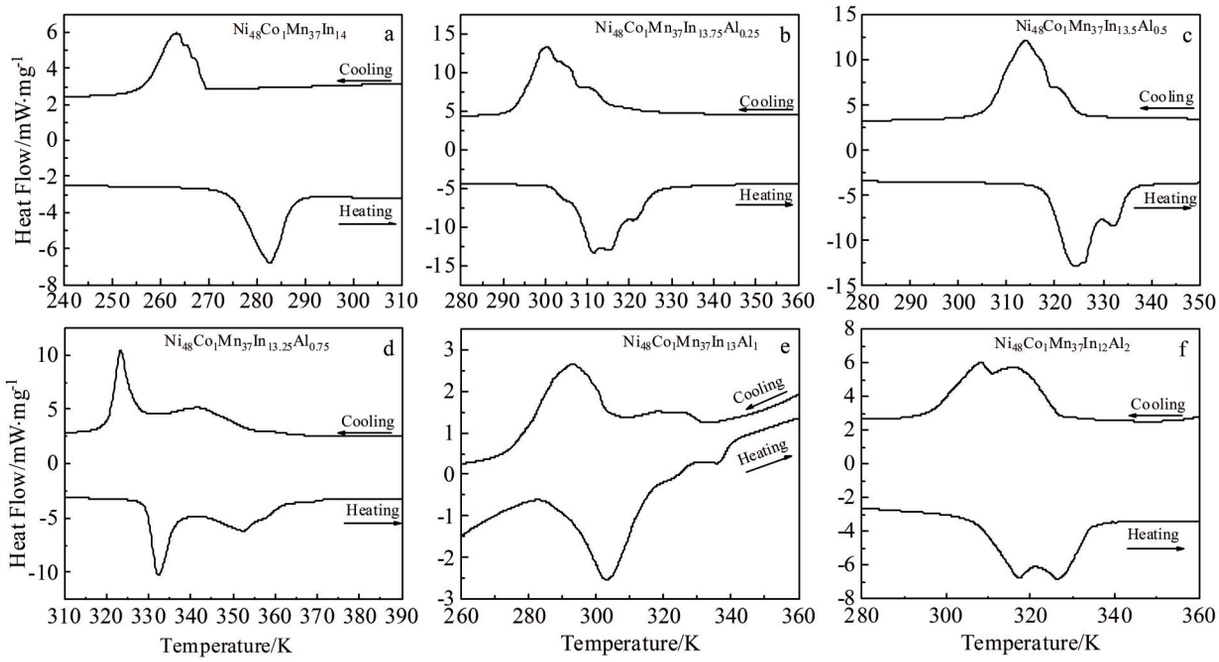

Fig.3 DSC curves of $Ni_{48}Co_1Mn_{37}In_{14-x}Al_x$ alloys: (a) x=0, (b) x=0.25, (c) x=0.5, (d) x=0.75, (e) x=1, and (f) x=2

Table 3 Characteristic temperatures of $Ni_{48}Co_1Mn_{37}In_{14-x}Al_x$ alloys

x	M_s/K	M_f/K	A_s/K	A_f/K	ΔT_{hys}/K
0	270	262	272	280	10
0.25	309	295	302	320	9
0.5	312	302	312	320	9
0.75	327	318	326	336	8.5
1	310	285	292	319	8
2	326	308	319	334	8

reduced to about 9 K. After doping with 2at% Al, the thermal hysteresis of the alloy sample continues to decrease to about 8 K, which is obviously smaller than that of other reported magnetic memory alloys. According to the geometric nonlinearity theory of martensitic transformation, the thermal hysteresis observed around the martensitic transformation is closely related to the geometric compatibility of the interface between austenite and martensite. When the intermediate eigenvalue (λ_2) of the transformation tensor is close to 1, the geometric compatibility of the interface between two phases of the alloy is good, and the thermal hysteresis of the transformation is small[11]. The $|\lambda_2-1|$=0.02 of alloy with 2at% Al is calculated, which shows that the martensitic transformation of the alloy has relatively good cycle stability and small thermal hysteresis, which is consistent with the DSC results.

The martensitic transformation temperature of $Ni_{48}Co_1Mn_{37}In_{14-x}Al_x$ alloys is shown in Fig. 4. With the increase in Al

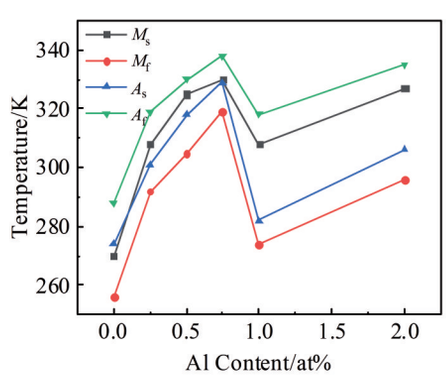

Fig.4 Effect of Al content on characteristic temperature of $Ni_{48}Co_1Mn_{37}In_{14-x}Al_x$ alloys

content from 0 to 2at% , the martensitic transformation temperature of the alloy increases first, then decreases and then continues to rise. When x=0, the starting temperature of martensitic transformation is below room temperature, 270 K. With the increase in Al content, the phase transition temperature of the sample increases. When x=0.75, M_s increases to 327 K, increased by 57 K compared with the M_s of undoped Al alloy. When x=2, the phase transition temperature of the alloy increases to 326 K, higher than room temperature. It indicates that in the process of replacing In with Al, the change of spacing between Mn-Mn atoms brings a certain chemical pressure[21]. The change of relative stability between austenite and martensite structure caused by lattice distortion leads to the shift of martensitic transformation temperature[22]. In addition, related studies have pointed out that the size of lattice constant and valence electron concentration (e/a) are the two main factors affecting the phase transformation temperature of NiMnX (X=In, Sn, Sb, Ga) alloy[6]. Generally, martensitic transformation temperature increases with decreasing lattice constant or increasing valence electron concentration. Al and In belong to the third main group, with the same valence electron concentration, and the change in martensitic transformation temperature can be attributed to the change in cell volume.

2.3 Mechanical properties of $Ni_{48}Co_1Mn_{37}In_{14-x}Al_x$ alloys

Fig.5 is the compressive stress-strain curve of $Ni_{48}Co_1Mn_{37}In_{14-x}Al_x$ alloy at room temperature. It can be seen that the doping of the Al element can significantly improve the compressive strength and fracture strain of the alloy. When the Al content is no more than 2at% , the compression deformation process of the test alloy can be divided into three stages: (1) elastic deformation with a linear correlation between stress and strain[23]; (2) when the stress reaches 125–300 MPa, there is an obvious yield platform because the orientation of martensite variants in the alloy grains tends to be consistent under stress, that is, the stress-strain platform is generated on the curve[24]; (3) plastic deformation with simultaneous increase in stress and strain until fracture.

Fig.6 shows the variation of compressive fracture strength and fracture strain of $Ni_{48}Co_1Mn_{37}In_{14-x}Al_x$ alloy with Al content. As can be seen from Fig. 6a, the fracture strength increases rapidly with the increase in Al content when Al content is lower than 0.75at% in the martensite state. When the Al content reaches 1at%, the fracture strength continues to increase slightly. When the Al content increases to 2at%, the compressive fracture strength of the alloy increases to 488 MPa, which is about 160% higher than that of the original $Ni_{48}Co_1Mn_{37}In_{14}$ alloy. Fig.6b shows the effect of Al content on the fracture strain of the alloy. When the Al content is lower than 0.5at%, the fracture strain increases rapidly and reaches the maximum value at 0.5at%, which increases from 5.46% to 6.76%. When the Al content is between 0.5at% and 2at%, the fracture strain shows a certain downward trend, but the overall fracture strain is higher than that of the undoped alloy.

In order to study the fracture mechanism of the alloy and to analyze the toughening mechanism, Fig. 7 shows the compression fracture morphology of $Ni_{48}Co_1Mn_{37}In_{14-x}Al_x$ alloy at room temperature. It can be seen that the grain size decreases significantly with the doping of the Al element. It can be seen from Fig.7a that the micro-fractures of the alloy doped with a trace amount of Al (0.25at%) is ice-sugar-like, with a smooth crystal surface and obvious cracks at the grain boundary. As indicated by the arrows, the microstructure is brittle fracture morphology, which is a typical intergranular fracture. At this time, the external force load of the alloy is directly borne by the grain boundary, and the grain boundary bonding force is weak, the strength is low, and the ductility is poor. When x= 0.5, the arrow in Fig. 7b shows that a small amount of elongated martensite laths appear on the grain surface, indicating that some intergranular cracks originate from the shrinkage of cell volume during martensite formation. At the same time, the circle in the figure shows that some ductile

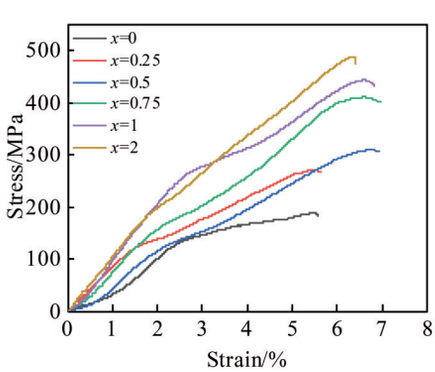

Fig.5 Compression stress-strain curves of $Ni_{48}Co_1Mn_{37}In_{14-x}Al_x$ alloys at room temperature

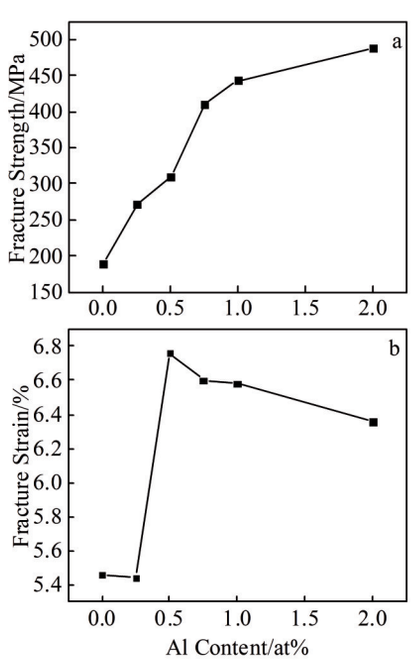

Fig.6 Effect of Al content on fracture strength (a) and fracture strain (b) of $Ni_{48}Co_1Mn_{37}In_{14-x}Al_x$ alloys

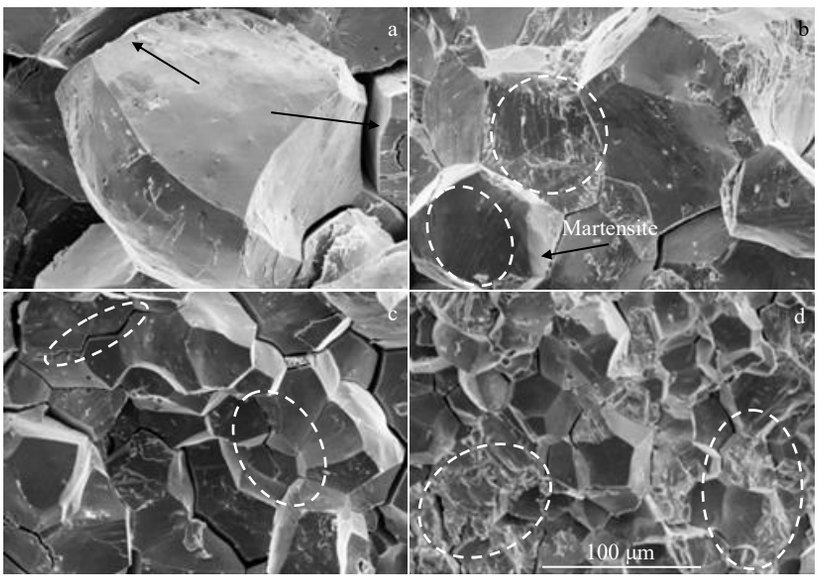

Fig.7 Compression fracture morphologies of $Ni_{48}Co_1Mn_{37}In_{14-x}Al_x$ alloys: (a) x=0.25, (b) x=0.5, (c) x=1, and (d) x=2

tearing traces appear in the grain, indicating that the plasticity of the alloy is improved. In the alloy doped with 1at% Al, as shown by the circle in Fig.7c, transgranular cracks can be seen in some regions, and the strength of the alloy continues to increase. Fig. 7d shows that the fracture toughness tearing edge of $Ni_{48}Co_1Mn_{37}In_{12}Al_2$ alloy increases, showing obvious transgranular fracture characteristics, indicating the existence of plastic deformation before fracture, with high strength and plasticity.

In summary, an appropriate amount of Al addition can significantly improve the compressive strength and compressive strain of NiCoMnIn alloy as well as the plasticity and toughness of the alloy. The main reasons for the improvement in mechanical properties of the alloy are the following two points. (1) From the microstructure and crystal structure of the alloy, it can be seen that Al plays an obvious role in fine-grain strengthening. By effectively dispersing the plastic deformation of the grain and reducing the stress concentration, the plasticity and toughness of the alloy are enhanced. (2) Al with a small atomic radius is solidified into the matrix, resulting in a certain degree of lattice distortion, reducing the dislocation degree of grain movement, and thus improving the strength of the alloy.

2.4 Corrosion resistance of $Ni_{48}Co_1Mn_{37}In_{14-x}Al_x$ alloys

Fig. 8 is the potentiodynamic polarization curves of $Ni_{48}Co_1Mn_{37}In_{14-x}Al_x$ alloys. It can be seen that the polarization curves of alloys with different compositions show similar changes. A current platform, namely the passivation region, can be seen in all anodic polarization curves. This is because the aluminum ions generated by the anodic dissolution reaction combine with the oxygen in the solution to form a dense alumina passivation film on the surface of the alloy. When the potential increases to about 0 V, the corrosion current density increases linearly, while the potential slowly increases. At this time, pitting corrosion will occur at the

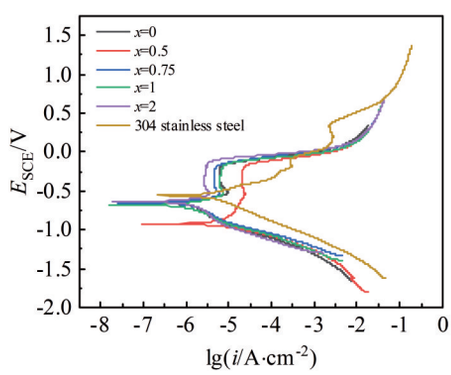

Fig.8 Polarization curves of $Ni_{48}Co_1Mn_{37}In_{14-x}Al_x$ alloy and 304 stainless steel

position where the protection of the passivation film on the alloy surface is weak, and the passivation film begins to be destroyed, showing over-passivation corrosion behavior.

The characteristic parameters of polarization curves obtained by Tafel fitting are shown in Table 4. The data show that with the increase in Al content, the self-corrosion potential and self-corrosion current of the material change, and the corrosion resistance of the alloy sample decreases first and then increases. According to Farady's second law, the corrosion rate of the sample has a linear relation with the current density corresponding to the corrosion potential[25]. The corrosion current density of the alloy with Al content of 0.5at% is the highest, and the self-corrosion potential is the most negative, indicating that the alloy has the largest corrosion tendency and the corrosion resistance decreases. The corrosion resistance of the alloy increases with increasing Al content, and the corrosion rate of the alloy with 2at% Al content is about 0.048 mm/a, which is 30% lower than that of $Ni_{48}Co_1Mn_{37}In_{14}$ under the same conditions. The results show that the corrosion resistance of the alloy is improved, which

Table 4 Fitting parameters of polarization curves of $Ni_{48}Co_1Mn_{37}In_{14-x}Al_x$ alloys and 304 stainless steel

Composition	E_{corr}/mV	I_{corr}/μA·cm^{-2}	Corrosion rate/ mm·a^{-1}
$Ni_{48}Co_1Mn_{37}In_{14}$	−652.7	1.493	0.069
$Ni_{48}Co_1Mn_{37}In_{13.5}Al_{0.5}$	−924.5	1.996	0.093
$Ni_{48}Co_1Mn_{37}In_{13.25}Al_{0.75}$	−653.5	1.319	0.061
$Ni_{48}Co_1Mn_{37}In_{13}Al_1$	−682.7	1.148	0.053
$Ni_{48}Co_1Mn_{37}In_{12}Al_2$	−639.4	1.038	0.048
304 Stainless Steel	−559.3	4.192	0.049

proves that the appropriate amount of Al element doping can effectively improve the corrosion resistance of the alloy. In order to further determine the corrosion resistance of the alloy system, the dynamic polarization curves of 304 stainless steel were measured under the same conditions, and the corresponding electrochemical parameters are listed in Table 4. By comparing the data, it can be found that the self-corrosion current density of Ni-Co-Mn-In-Al alloy is significantly lower than that of 304 stainless steel, and the corrosion rate of $Ni_{48}Co_1Mn_{37}In_{12}Al_2$ alloy is even lower than that of 304 stainless steel. Through analysis, it can be concluded that the corrosion resistance of the alloy after replacing In with 2at% Al is close to that of 304 stainless steel[26].

3 Conclusions

1) For $Ni_{48}Co_1Mn_{37}In_{14-x}Al_x$ (x=0.25, 0.5, 1, 2, at%) alloy, with the increase in Al content, the grain size is obviously refined. When Al content is 2at% , the average grain size decreases from 350 μm to about 10 μm. When the Al content is between 0.25at% and 2at% , the second phase is not observed in the alloy. The metal Al is completely dissolved in the matrix, and the solid solubility in the alloy also increases with the increase of Al in Al content. When 2at% Al is used to replace In, the solid solubility of Al in the matrix is close to 2at%.

2) The crystal structure of $Ni_{48}Co_1Mn_{37}In_{14}$ alloy at room temperature is a mixed structure of cubic $L2_1$ austenite and monoclinic 6M modulated martensite. When the Al content increases from 0.25at% to 2at% , the austenite phase disappears, and the alloy presents a single-phase monoclinic 6M martensite. With the increase in Al content, the lattice constant b decreases, and the cell volume decreases as a whole.

3) The $Ni_{48}Co_1Mn_{37}In_{14-x}Al_x$ alloy experiences one-step thermoelastic martensitic transformation during the heating and cooling process. When the Al content increases from 0at% to 2at% , the martensitic transformation temperature of the alloy system shows an overall upward trend, from 270 K to 326 K, and the thermal hysteresis also decreases from 10 K to 8 K.

4) With the substitution of Al for In, the mechanical properties of the Ni-Co-Mn-In alloy are significantly improved. The compressive fracture strength of $Ni_{48}Co_1Mn_{37}In_{12}Al_2$ reaches 488 MPa, which is 160% higher than that of $Ni_{48}Co_1Mn_{37}In_{14}$, and the compressive strain also increases from 5.46% to 6.36%, which is due to the effect of Al doping on fine grain strengthening and solid solution strengthening. The compression fracture morphology of quaternary $Ni_{48}Co_1Mn_{37}In_{14}$ alloy is a single intergranular fracture, showing high brittleness. After doping of trace Al element, transgranular fracture characteristics appear, and the fracture mechanism gradually evolves from single brittle fracture to plastic fracture, with higher plasticity and toughness.

5) With the substitution of Al for In, the corrosion resistance of the alloy in artificial seawater solution shows an overall increasing trend. The corrosion resistance rate of $Ni_{48}Co_1Mn_{37}In_{12}Al_2$ alloy is 0.048 mm/a, which is only 70% of that of the undoped alloy, showing good corrosion resistance, and its corrosion resistance is close to that of 304 stainless steel.

References

1 Liu Enke, Liu Jian, Wang Dunhui. *Scientia Sinica (Physica, Mechanica & Astronomica)*[J], 2021, 51(6): 5

2 Kainuma R, Imano Y, Ito W *et al. Nature*[J], 2006, 439(7079): 957

3 Antoni Planes, Lluís Mansosa, Mehmet Acet. *Journal of Physics: Conden Matter*[J], 2009, 21(23): 233 201

4 Li Zhenzhuang, Li Zongbin, Yang Bo *et al. Material Science and Engineering A*[J], 2020, 780: 139 170

5 Monroe J A, Karaman I, Basaran B *et al. Acta Materialia*[J], 2012, 60(20): 6883

6 Huang Xiaoming, Zhao Ying, Yan Haile *et al. Journal of Alloys and Compounds*[J], 2022, 889: 161 652

7 Kirat Gokhan, Ali AksanMehmet. *Journal of Magnetism and Magnetic Materials*[J], 2021, 529: 167 858

8 Zhou Z N, Akamine H, Li J *et al. Journal of Alloys and Compounds*[J], 2020, 817: 153 150

9 Aslani Amir, Ghahremani Mohammadreza, Bennett Lawrence H. *IEEE Transactions on Magnetics*[J], 2021, 57(2): 1

10 Wang Limin, Li Zongbin, Yang Jiajing *et al. Intermetallics*[J], 2020, 125: 106 888

11 Yan Haile, Huang Xiaoming, Yang Jinhai *et al. Intermetallics*[J], 2021, 130: 107 063

12 He Xijia, Zhang Yuanlei, Wei Shengxian *et al. Journal of Physics D: Applied Physics*[J], 2021, 54(16): 165 001

13 Prabu S S Mani, Perugu Chandra S, Jangde Ashutosh *et al. Surface and Coatings Technology*[J], 2020, 402: 126 495

14 Gebert A, Roth S, Oswald S *et al. Corrosion Science*[J], 2009, 51(5): 1163

15 Liu Ming, Li Jun, Zhang Yanxiao *et al. Rare Metal Materials and Engineering*[J], 2021, 50(11): 4165

16 Li Hang, Meng Xionglong, Cai Wei. *Materials Science and Engineering A*[J], 2018, 725: 359

17 Matyja Edyta, Prusik Krystian, Zubko Maciej *et al. Journal of Alloys and Compounds*[J], 2020, 859: 157 841
18 Bai Jing, Liu Die, Gu Jianglong *et al. Journal of Materials Science & Technology*[J], 2021, 74: 46
19 Cong D Y, Huang L, Hardy V *et al. Acta Materialia*[J], 2018, 146: 142
20 Li Yuanyuan, Zhang Ziyi, Guan Jiahao *et al. Rare Metal Materials and Engineering*[J], 2021, 50(5): 1513
21 Devi P, Salazar Mejía C, Ghorbani Zavareh M *et al. Physical Review Materials*[J], 2019, 3(6): 62 401
22 Cicek M M, Saritas S, Yildirim O *et al. Journal of Alloys and Compounds*[J], 2020, 845: 155 493
23 Zhang Yajiu, Guo Jinpei, Zhong Minting *et al. Journal of Magnetism and Magnetic Materials*[J], 2021, 521(2): 167 540
24 Aydogdu Y, Turabi A S, Kok M *et al. Journal of Alloys and Compounds*[J], 2016, 683: 339
25 Qu Qing, Li Shunling, Li Lei *et al. Corrosion Science*[J], 2017, 118: 12
26 Zhao Yan, Wang Xu, Chen Dayu *et al. Rare Metal Materials and Engineering*[J], 2023, 52(2): 535

$Ni_{48}Co_1Mn_{37}In_{14-x}Al_x$磁性记忆合金马氏体相变、力学性能和耐腐蚀性能

高　丽，辛向阳，刘紫莉，胡少辉，廖华玉，徐阳睿
(上海海洋大学 工程学院，上海 201306)

摘　要：采用电弧熔炼的材料制备方法，研究了微量的主族元素Al掺杂对$Ni_{48}Co_1Mn_{37}In_{14-x}Al_x$ ($0\leqslant x\leqslant 2$)磁性形状记忆合金显微组织、晶体结构、马氏体相变、力学性能和耐腐蚀性能的影响。结果表明：用Al替代部分In，合金的晶粒尺寸明显减小，掺杂2at%的Al元素，平均晶粒尺寸缩小到10 μm左右，大约为未掺杂样品的三十五分之一；当Al掺杂量在0.25at%~2at%时，金属Al完全固溶到基体中，而且Al在合金中的固溶度随掺杂量的增加有所提升，当Al掺杂量为2at%时，Al在基体中的固溶度接近2at%；随着Al对In的取代，室温下合金由$L2_1$立方奥氏体与单斜6M马氏体的两相结构转变为单一的6M调制马氏体相结构，晶胞体积逐渐减小，马氏体相变温度呈现上升趋势；合金抗压强度不断增大，$Ni_{48}Co_1Mn_{37}In_{12}Al_2$的抗压缩断裂强度与$Ni_{48}Co_1Mn_{37}In_{14}$相比提高了160%，压缩应变也由5.46%增加到6.36%；适量的Al替代In后，合金在人工海水中的耐腐蚀性能总体呈现不断增强的趋势，$Ni_{48}Co_1Mn_{37}In_{12}Al_2$合金的耐腐蚀性能明显高于$Ni_{48}Co_1Mn_{37}In_{14}$合金，且其耐腐蚀性接近于304不锈钢。

关键词：磁性形状记忆合金；金属Al掺杂；马氏体相变；力学性能；耐腐蚀性能

作者简介：高　丽，女，博士，教授，上海海洋大学工程学院，上海 201306，E-mail：lgao@shou.edu.cn